# Growth mechanism of thin silicon oxide films on Si(100) studied by medium-energy ion scattering

E. P. Gusev
*Department of Chemistry and Laboratory for Surface Modification, Rutgers University, P.O. Box 939, Piscataway, New Jersey 08855*

H. C. Lu and T. Gustafsson
*Department of Physics and Astronomy and Laboratory for Surface Modification, Rutgers University, P.O. Box 849, Piscataway, New Jersey 08855*

E. Garfunkel
*Department of Chemistry and Laboratory for Surface Modification, Rutgers University, P.O. Box 939, Piscataway, New Jersey 08855*
(Received 27 December 1994)

The growth of ultrathin oxide films by the thermal oxidation of Si(100) at 1020–1170 K and in $10^{-1}-10^{-3}$ Torr $O_2$ pressure has been studied by high-resolution medium-energy ion-scattering spectroscopy (MEIS). To develop a fundamental understanding of very thin oxide film growth, we utilize sequential isotopic exposures ($^{18}O_2$ followed by $^{16}O_2$). MEIS readily distinguishes $^{18}O$ from $^{16}O$ and the depth distribution for both species can be determined quantitatively with high accuracy. Our results show that the traditional phenomenological models for silicon oxidation cannot be applied to the initial oxidation. For very thin oxide films (15–25 Å), we find overlapping isotope depth profiles in the film. For thicker films (> 40 Å), we find that several key aspects of the Deal-Grove model (oxygen diffusion to the Si-$SiO_2$ interface and oxide formation at and/or near that interface) are consistent with our results. We also observe $^{18}O$ loss from the surface after reoxidation in $^{16}O_2$. The complex oxidation behavior during the initial oxidation is likely to be a combination of interfacial, near-interfacial, and surface reactions.

## I. INTRODUCTION

The oxidation of metals and semiconductors is one of the oldest and most thoroughly studied class of reactions in materials science.[1–15] Most work has concentrated on either the oxide growth mechanism for relatively thick films (100 Å – 10 μm)[1–3,6,7,11,12] or the oxygen-surface interaction in the limit of submonolayer coverage.[4,5,14,16–18] The oxidation mechanism in the critical 10–100-Å range (the initial oxidation) is much less well understood. The purpose of this paper is to examine the microscopic mechanism for oxide film growth on silicon in the range 15–50 Å.

Ultrathin-film silicon oxidation is now of particular relevance to the microelectronics industry as the thickness of metal-oxide-semiconductor gate oxides drops well below 100 Å. However, despite considerable effort, there is no general agreement concerning the growth mechanism for these films.[6,11,12,14] Oxidation of relatively thick (> 100-Å) films is known to be described by the Deal-Grove model.[19] According to this "linear-parabolic" model, the oxide grows via molecular oxygen diffusion through the oxide film and molecular oxygen reaction with silicon at the Si/$SiO_2$ interface. In the limit of thick films, the oxide film growth rate is limited by oxygen diffusion through the film resulting in a parabolic dependence of oxidation time versus oxide thickness. When the oxide is very thin, oxygen diffusion is fast compared to the interfacial reaction rate, and hence the latter controls the oxidation kinetics. Assuming first-order reaction kinetics at the interface, Deal and Grove deduced a linear relationship between oxide thickness and oxidation time in this limit.[19]

It has been shown, however, that the oxidation kinetics for ultrathin films are faster than would be expected from a linear relationship.[8,9,11,12,20] Several phenomenological models, such as the parallel oxidation model,[21] the blocking layer model,[9,22] and others, have been proposed to account for this deviation. The experimental support for these models comes mostly from kinetic data. The idea of the reactive layer[12,23] was advanced later as an attempt to integrate the observation of microcrystallinity near the interface,[24] a thin transition region of nonstoichiometric oxide[16,25–27] and deviations of the oxygen isotope distributions from the Deal-Grove mechanism, as inferred from experiments by hydrofluoric acid (HF) etching in combination with nuclear reaction analysis (NRA) with oxygen isotopes.[24] In contrast to the Deal-Grove model, the reactive layer model posits that oxidation takes place at the top (internal) surface of a "reactive layer" between crystalline Si and amorphous $SiO_2$. The reactive layer was defined as a thin oxide layer (estimated to be ~10–20 Å thick) near the interface that is impermeable to interstitial $O_2$ diffusion. In this paper, our results will be mainly compared with the Deal-Grove and reactive layer models, because they represent two qualitatively different views of the oxidation reaction. Most other models attempt to modify either the mechanism of oxygen diffusion or the reaction at the interface, and can, therefore, be considered as modifications of the original Deal-Grove idea.

Some of the phenomenological models fit the experimental data on oxidation kinetics quite satisfactorily with

0163-1829/95/52(3)/1759(17)/$06.00  ©1995 The American Physical Society

a large number of fitting parameters. Unfortunately, most of the models do not have direct experimental support; an analysis of kinetic results alone does not allow one to conclusively distinguish between models. Therefore, additional experiments must be performed in order to shed light on the complex mechanism of the initial stages of silicon oxidation.

The Deal-Grove model considers the reaction at the interface as a first-order reaction between silicon and molecular oxygen. Other models[21] consider, for example, oxygen dissociation at the interface and again a first-order reaction of atomic oxygen with silicon. Such "gas-phase" considerations ignore the spatial (lateral and vertical) aspects of the oxidation at the interface between two solids and the role of the substrate silicon atoms. In particular, they imply random reaction of oxygen molecules with silicon substrate atoms at the interface, although this cannot explain the abrupt oxide/silicon interface after oxidation. There is intense discussion in the literature[14,28–36] on the issue of lateral homogeneity during the initial oxidation: Does the oxide growth proceed uniformly on the surface in a layer-by-layer fashion, or are 3D islands of silicon oxide formed? Some photoemission[28–30,35] and high-resolution transmission electron microscopy (HRTEM) (Refs. 31–34) results were interpreted as evidence for layer-by-layer growth. However, three-dimensional (3D) island growth has also been claimed to occur under certain oxidation conditions.[13,28,29]

It is generally agreed that there is a transition region (of altered structure and stoichiometry) between crystalline silicon and $a$-$SiO_2$.[9,11,14,16,17,25,27,37–40] The thickness of this region has been reported to be from 5 to 30 Å, depending on oxidation procedures, oxide thickness, and the probing technique. At the atomic scale, some view the transition region as consisting of silicon atoms in intermediate oxidation (suboxide) states, $Si^{n+}$ ($n=1$, 2, 3),[16,17,25] although this interpretation is now under debate.[41–43] Other models emphasize structural order[44,45] and stress anomalies[9,46] in the transition region. Furthermore, relatively little is known about the role of the transition region in the initial oxidation. According to the reactive layer model,[12,23] silicon atoms diffuse through the thin reactive layer and react with oxygen on top of this layer, forming the $SiO_2$ phase. Tiller and others[47–49] have suggested that interstitial silicon generation takes place during the oxidation reaction at the interface. These silicon atoms subsequently diffuse into the oxide, where they interact with oxygen leading to oxidation in the near-interfacial region. However, little experimental evidence has been reported to support this idea.

Silicon oxide growth is known to be temperature and pressure dependent. In addition to temperature and pressure variations in the rate of oxide growth, there is a region in the ($P$-$T$) phase diagram, where SiO desorption (surface etching) takes place. The low-temperature high-pressure part of the phase diagram is characteristic of oxide growth, while SiO desorption occurs under high-temperature low-pressure conditions.[36,50–53] In one case, Tromp and co-workers[54] have shown that high-temperature annealing of a 100-Å oxide under UHV conditions results in oxide decomposition and SiO desorption. Little is known concerning the existence of SiO desorption or $O_2$ exchange under oxide growth conditions.

In this paper, we discuss the microscopic mechanism(s) of very thin oxide growth during thermal "dry" oxidation, and go beyond a simple phenomenological kinetic description. Key problems we address are as follows: (i) Where does the oxidation take place? (ii) Does the Deal-Grove model apply to 15–50-Å films? (iii) What is the structure and stoichiometry in the transition region and what is its role in the initial oxidation? (iv) Does oxygen leave the oxide during film growth?

We use medium-energy ion scattering (MEIS), a low-energy (50–300-keV) high-resolution version of Rutherford backscattering spectroscopy (RBS),[55–58] to study silicon exposed sequentially to $^{18}O_2$ and $^{16}O_2$ isotopes as our main experimental tool. Due to the high-energy resolution of MEIS, we can quantitatively determine the depth distribution of the two isotopes with high accuracy. Our preliminary results have demonstrated the power of this method.[59] It should be noted that ion scattering has been successfully used to study clean silicon surfaces[60] and relatively thick oxide films.[38,54,61] For example, Feldman and co-workers showed with RBS that the transition region between crystalline Si(100) or Si(111) and the $SiO_2$ layer for thermally grown oxides consisted of about a 5-Å nonstoichiometric oxide near the interface and one or two reconstructed silicon layers.[37,38,61–63]

Isotopic substitution has been employed in the past to study the oxidation mechanism in conjunction with secondary ion mass spectrometry, and NRA with HF etch profiling.[24,64–71] These studies helped confirm that thick oxide film growth does follow Deal-Grove kinetics. However, the limitations and uncertainties in the depth resolution of these techniques make meaningful analysis in the ultrathin film regime (15–50 Å) difficult.

This paper is organized as follows. In Sec. II, we describe the experimental setup and discuss the idea of isotope depth profiling with MEIS as a method to study ultrathin oxide growth. We then present experimental results (Sec. III). A key qualitative result for very thin ($<25$ Å) oxides is that we observe similar distributions for both isotopes after sequential oxidation, directly implying non-Deal-Grove behavior. Isotope profiles in the growing oxide films are compared with known phenomenological models of silicon oxidation (Sec. IV A). We show in this section that neither the Deal-Grove model (and its subsequent variants) nor the reactive layer model can be applied for very thin ($<25$ Å) films, and we discuss (Sec. IV B) other possible mechanisms for oxide growth during the initial oxidation. Some details of the ion-scattering analysis and the procedure for spectral simulation are given in the Appendix.

## II. EXPERIMENT

We have employed the unique strengths of MEIS (mass-sensitivity, high depth resolution, and quantitative analysis) in our experiments. In MEIS [Fig. 1(a)], a monoenergetic beam of charged particles scatter from

surface and near surface atoms. The energy spectra of the scattered particles provides a depth and composition profile of the near surface region. To eliminate the background scattering from atoms in the crystalline Si substrate, the experiments are usually performed in a channeling geometry with the beam aligned along one of the major crystallographic directions or even in a double-aligned geometry (where the detector axis is also aligned with a crystallographic axis, i.e., channeling and blocking).[56] Energy spectra of backscattered particles can be converted into a mass scale through a kinematic factor. The kinematic factor is a function of target atom mass and scattering angle, and can be calculated within a binary collision model (using classical momentum and energy conservation). In our case, a 97.2-keV incident-proton beam was aligned with the [100] direction of silicon and the backscattered protons were collected around 125.0° scattering angle in the (110) plane (double alignment geometry). Our high-resolution toroidal electrostatic energy analyzer is equipped with channel plates and a 2D position sensitive detector, and collects data simultaneously over a wide range of energy ($\sim$1.6 keV at $\sim$80 keV) and angles ($\sim$22°).[72] Since the scattered particles lose energy via inelastic electronic excitations as they travel through the film, species that lie below the surface can be distinguished from the ones at the surface by their relative energy loss. For 100-keV protons, the energy loss in Si is about 12 eV/Å.[73] Our detector gives us $\sim$110-eV resolution for $\sim$80-keV protons. This converts to a $\sim$5-Å effective depth resolution for thin oxide films under our scattering conditions.

It is useful to point out that the efficiency of the channel plates in the detector can be affected by oxygen used in the oxidation cycles. We found changes (sometimes as large as 20%) after exposing the channel plates to oxygen at pressures higher than $10^{-6}$ Torr. Fortunately, this problem does not effect the present result, as most of our oxidation is performed in the sample preparation chamber and, in addition, an overall efficiency change can be corrected with the known Si density in the substrate or $SiO_2$ layer. But any experiment that is based on information concerning absolute coverages or accurate angular spectra need to carefully consider this problem.

The principles of our isotopic oxidation experiments are demonstrated in Fig. 1. In the simple case of oxidation in the naturally predominant oxygen isotope ($^{16}O_2$), only one oxygen peak is seen in the MEIS channeling energy spectrum [Fig. 1(a)]. The high-energy (leading) edge of the peak corresponds to the oxygen atoms at the surface, and its energy is given by the kinematic factor; at lower energies, we observe ions scattered from oxygen atoms closer to the Si-$SiO_2$ interface. The thicker the film, the more energy the protons lose on their way to and from the interface, and the broader the peak. Under channeling conditions, silicon layers deep in the crystalline substrate are invisible to the proton beam due to shadowing. As a result, the energy spectrum for protons scattered from silicon atoms also consists of a relatively narrow peak. The peak is due to protons scattered from silicon atoms in the amorphous oxide and in a few substrate layers near the interface. Some of the substrate silicon atoms near the interface are still visible to the incident protons, due to thermal vibrations and possible distortions near the interface caused by the presence of the oxide layer. For this reason, the silicon peak is slightly broader than the oxygen peak, whose width is solely determined by the oxide thickness. The silicon peak has a higher intensity than the oxygen peak, because the scattering cross section for silicon is about three times greater than for oxygen.

To illustrate the type of MEIS spectra anticipated after sequential isotopic oxidation, we consider two limiting cases. For a thin film, the MEIS spectrum should show two separate oxygen peaks: $^{18}O$ at higher energies and $^{16}O$ at lower energies. If the initial oxidation followed the Deal-Grove model, one would expect an $Si^{18}O_2$ oxide mainly near the surface (as the $^{18}O_2$ exposure was performed first) and an $^{16}O$-containing oxide near the interface [Fig. 1(b)]. Since $^{18}O$ is at the surface, its leading edge should match the energy calculated within the binary collision model (indicated by dashed lines). The protons lose energy traveling through the $Si^{18}O_2$ layer before (and after) they reach the $Si^{16}O_2$ region, resulting in a shift of the leading edge of the $^{16}O$ peak with respect to

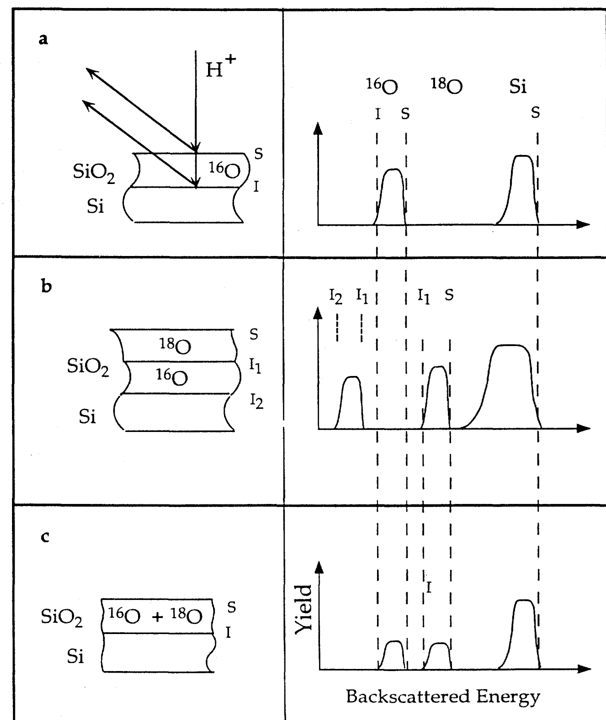


FIG. 1. Schematic representation of some possible isotopic distributions (left) and MEIS channeling energy spectra (right) corresponding to (a) uniform oxidation in $^{16}O_2$, (b) the Deal-Grove model, and (c) uniform isotopic mixing. The scattering conditions used in our experiments are shown in (a). The symbol "*S*" denotes the oxide surface, "*I*" represents the interface(s).

the binary collision model edge. This shift is proportional to the thickness of the $Si^{18}O_2$ layer. The widths of both peaks are also proportional to the respective layer thicknesses.

Very different spectra would be expected if the oxidation took place uniformly throughout the growing oxide film, as this would result in a uniform isotopic mixture [Fig. 1(c)]. In this case, both isotopes are on the surface after sequential oxidation. Therefore, the energies of their leading edges would be given by the binary collision model. Both peaks would have the same width because the isotopes have the same depth distributions. Thus, by simply examining the MEIS leading edge positions and the peak widths, one can begin to model the oxide growth mechanism. More detailed information, in particular the depth profiles, can be deduced from modeling, as demonstrated in Sec. IV.

The cross section in MEIS is proportional to the second power of the atomic numbers and, therefore, is relatively small for proton-oxygen scattering. Thus, long data acquisition times (or high proton doses) are required to obtain satisfactory statistics. Unfortunately, increasing the ion dose may cause beam-induced damage to the film. To minimize the dose, and hence the damage, on each beam spot ($1.00\times0.07$ mm), we scan across the sample by using a stepper-motor-driven manipulator. Only one sample was needed to collect data with good statistics. We also averaged data points in an energy spectrum over six angular channels ($\sim1°$ width) to enhance our signal-to-noise ratio. In this paper, an energy spectrum nominally taken at 115° therefore refers to data collected at scattering angles from 114.5° to 115.5°. We monitored ion-induced damage by measuring, in a separate experiment, the change of the silicon peak area as a function of the proton dose. The increase in the surface peak area does not exceed 5% for the dose used ($\sim3\times10^{16}$ protons $cm^{-2}$). This result is consistent with an estimate of the total number of displaced atoms calculated within Kinchin-Pease cascade theory ($\sim5.4\%$ for silicon, and $\sim3.5\%$ for oxygen).[56,74]

As a complement to MEIS, low-energy ion scattering (LEIS) ($He^+$, 1–1.5 keV, scattering angle 145°) was used to determined the isotopic composition in the outermost oxide layer. Because of the high neutralization probability of $He^+$ in this energy range, only helium ions scattered from the first surface layer survive as ions and are detected; this is the reason for the extremely high surface specificity of this method.[75,76] We have also employed x-ray-photoemission spectroscopy (XPS) with a Mg $K\alpha$ source to provide information on the oxidation states of silicon atoms in the oxide and as an additional tool to measure oxide thickness. All spectra were taken at room temperature in UHV chambers with a base pressure of about $10^{-10}$ Torr. Spectroscopic ellipsometry was used to compliment our results on the thickness of the stoichiometric $SiO_2$ and the transition region near the interface. These measurements were performed using UVISEL ellipsometer (Instruments S.A., Inc.).

We used *n*-type Si(100) samples ($\sim20\times8$ mm). They were cleaned in methanol, rinsed in water, and then heated by a direct current in UHV. The samples and sample holder were first degassed at 600–800 K for approximately 40–50 h. This was followed by several flashes to $\sim$1250–1350 K for 30–120 sec. The pressure rose during the high-temperature flashes, but was always less than $2\times10^{-9}$ Torr. This procedure resulted in a clean Si surface as determined by low-energy electron diffraction [$(2\times1)$ pattern], MEIS and XPS. We concentrated our efforts on oxide films grown *in situ* at temperatures from 1020 to 1170 K, the temperature range of silicon oxide growth for many industrial applications, and oxygen pressures of $10^{-3}$–$10^{-1}$ Torr. The sample temperature was measured by an optical pyrometer calibrated with a thermocouple. The difference between thermocouple and pyrometer readings was less than 5%. The final thickness of the oxides varied from 15 to 50 Å, depending on oxidation temperature, pressure, and time. Research grade (99.995% purity) oxygen was used. Samples were first oxidized in $^{18}O_2$ ($^{18}O_2$ isotopic concentration $\sim98.0\%$) and then reoxidized in natural oxygen ($^{16}O_2$ isotopic concentration 99.8%). Both isotopes were admitted into a preparation (oxidation) chamber in which the background vacuum was in the $10^{-9}$-Torr range. A liquid-nitrogen trap was used to reduce the water content of the background gas. To minimize tantalum diffusion from the sample holder during high-temperature oxidation,[77] we put silicon pads ($\sim0.4$ mm thick) between the front of sample and the tantalum clips. The tantalum concentration on the surface was near the limit of MEIS detection (for our conditions less than 0.5% of a monolayer of Ta). A second set of samples, having a uniform 50-Å $Si^{16}O_2$ layer, were produced in a commercial fab facility at IBM (1 atm, 1070 K). They are employed in studying the oxide structure of 50–60-Å films. We also use these samples (reoxidized in $^{18}O_2$) to address the growth mechanism for thicker (> 50 Å) films. Results of this study will be published separately.[78]

## III. RESULTS

In this section, we show MEIS, LEIS, and XPS results for films sequentially grown in $^{18}O_2$ and $^{16}O_2$. To develop a more complete picture of the oxidation process, we have performed measurements at various points in the complex pressure, temperature, and time phase space.

Figure 2(a) is an MEIS spectrum for a thin oxide first grown in $^{18}O_2$ (70 min), then in $^{16}O_2$ (120 min), at 1120 K and $10^{-3}$ Torr. (All MEIS spectra in this paper taken under channeling conditions are shown after subtraction of a very low background.) The thickness of the final oxide film is about 20 Å, as determined by MEIS (Sec. IV) and XPS (see below). Two well-separated peaks corresponding to protons scattered from $^{16}O$ and $^{18}O$ are seen in the spectrum. The proton energies corresponding to the leading edges of the peaks, 81.3 keV for $^{16}O$ and 83.0 keV for $^{18}O$, are in excellent agreement with binary collision model calculations (81.3 and 83.0 keV, respectively), which means that both oxygen isotopes are located on the oxide surface. If either isotope was located completely below the surface, the result would be an additional energy loss for protons scattered from that isotope and, as a result, the high-energy edge should shift to a lower

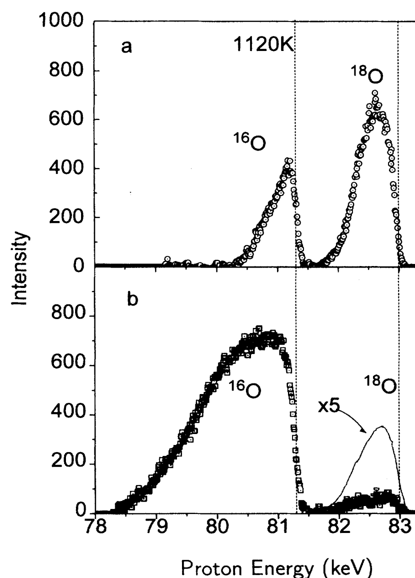


FIG. 2. MEIS energy spectra at a scattering angle of 115°. The oxidation conditions were (a) 70 min in $^{18}O_2$ followed by 120 min in $^{16}O_2$ at 1120 K and $\sim 10^{-3}$ Torr; and (b) 100 min in $^{18}O_2$ at 1080 K and $\sim 10^{-3}$ Torr followed by 120 min in $^{16}O_2$ at 1120 K and $\sim 10^{-1}$ Torr. The dashed lines show the energies for both isotopes calculated within the binary collision model. The incident-proton energy is 97.2 keV. Intensity is plotted in arbitrary units.

value [Fig. 1(b)]. We did not observe such a shift for this thin oxide. In addition, the peak widths for both isotopes are fairly similar, indicating that the distribution of the $^{18}$O and $^{16}$O regions are similar (since the peak widths are mainly determined by the film thickness), despite the fact that the isotopes were exposed sequentially [Fig. 2(a)]. A closer inspection shows that the peak shapes are slightly different. If we compare their full width at half maximum (FWHM, $\Delta_{1/2}$), the peak corresponding to $^{18}$O ($\Delta_{1/2}=0.63$ keV) is slightly broader than the $^{16}$O peak (0.50 keV). The difference in width gets even smaller at intensities lower than half maximum.

In Fig. 2(b), we present a MEIS spectrum for a thicker film, $\sim 50$ Å, grown first in $^{18}O_2$ (1080 K $10^{-3}$ Torr) for 100 min and then in $^{16}O_2$ (1120 K, $\sim 10^{-1}$ Torr) for 120 min. Again, the leading edges of the peaks corresponding to $^{16}$O and $^{18}$O atoms (81.3 and 83.0 keV, respectively) are those expected from the binary collision model (81.3 and 83.0 keV). Thus, both isotopes are present on the oxide surface, as with the thinner oxide. However, now the peaks have different shapes and widths, implying different depth distributions for the isotopes in the final oxide. The $^{18}$O peak FWHM of 0.60 keV is close to that corresponding to the $\sim 20$-Å oxide, whereas the $^{16}$O peak has a width of 1.68 keV ($\sim 50$ Å). Therefore the 50-Å oxide consists of an overlapped $^{16}$O and $^{18}$O oxide layer near the oxide-vacuum surface (analogous to that observed above in the 20-Å oxide), and a thicker $^{16}$O-containing layer underneath, adjoining the $Si/SiO_2$ interface. The areas under the peaks are proportional to the total amount of the isotopes in the film. For thicker films, the area under the $^{18}$O peak is much smaller than for 20-Å oxide [cf. Figs. 2(a) and 2(b)], indicating a smaller amount of this isotope in the thicker film. The fact that both isotopes are on the oxide surface after sequential oxidation is also confirmed by LEIS (Fig. 3), where both oxygen masses are seen in the spectrum after oxidation.

One should keep in mind that peaks in MEIS are always asymmetric and are not analogous to those observed in more traditional spectroscopies; actually, the concept of a FWHM is not very meaningful in our application of MEIS. Instead, we use an energy-spectra simulation program (similar to that used in RBS, see the Appendix) to find the isotopic distribution in the film.

The Si $2p$ XPS photoelectron spectra for these 20- and 50-Å films are shown in Fig. 4. Two peaks are seen in the photoelectron spectra. The peak at $\sim 99$ eV, the only one seen after sample cleaning, corresponds to substrate silicon atoms. The other photoemission peak is shifted by $\sim 4$ eV towards higher binding energy, and results from fully oxidized silicon atoms, $Si^{4+}$.[13,14,16–18,25–27,29,79,80] The ratio of the intensity from oxidized silicon atoms, $I_{ox}$, to the intensity from the substrate, $I_{Si}$, is used to determine the oxide thickness, $x$, according to the conventional formula[16,17]

$$x=\lambda \ln[(I_{ox}/I_{Si})(I_0/I_\infty)+1] , \quad (1)$$

where $\lambda$ is the Si $2p$ photoelectron escape length in the oxide, $I_0$ and $I_\infty$ are the Si $2p$ photoemission intensities for bulk silicon oxide and bulk silicon, respectively ($I_0/I_\infty=1.22$ for the Mg $K\alpha$ source[17]), and the photoelectron takeoff angle is normal to the surface. The problem in using this formula for determining the thickness is that the values of $\lambda$ for the Si $2p$ state reported for Mg $K\alpha$ radiation differ significantly, ranging from 21 to 35

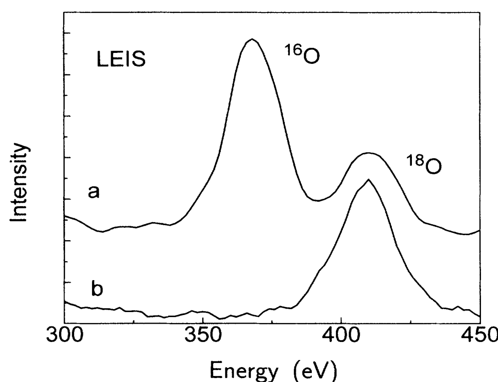


FIG. 3. LEIS spectra after (a) 100-min oxidation in $^{18}O_2$ at 1080 K and $\sim 10^{-3}$ Torr, and (b) reoxidation in $^{16}O_2$ for 120 min at 1120 K and $\sim 10^{-1}$ Torr. The primary energy of $He^+$ beam was 1.0 keV and the scattering angle 145°.

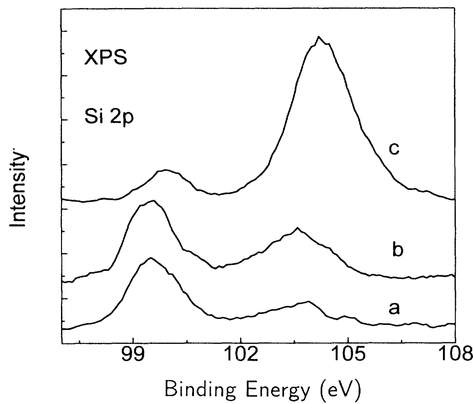


FIG. 4. Si $2p$ photoemission spectra after (a) 100 min oxidation in $^{18}O_2$ at 1080 K and $\sim 10^{-3}$ Torr, (b) reoxidation in $^{16}O_2$ for 120 min at 1120 K and $\sim 10^{-3}$ Torr, and (c) 120 min reoxidation in $^{16}O_2$ at 1120 K and $\sim 10^{-1}$ Torr.

Å.[81–83] We choose $\lambda = 30$ Å, based on a recent study calibrated with ellipsometry and RBS.[82] With this choice of $\lambda$, the Si $2p$ spectra shown in Fig. 4(b) and 4(c) correspond to oxide thicknesses of $\sim 20$ and $\sim 51$ Å, respectively.

We have also performed experiments at 1020 and 1170 K in order to understand if this overlap in the depth profiles of oxygen isotopes observed for the 20-Å oxide at 1120 K and the transition to (near) interface growth for thicker films holds under other oxidation (temperature and pressure) conditions. Figure 5 shows the evolution of MEIS spectra during oxidation at 1170 K and $10^{-2}$ Torr for increasing oxidation time. For all three samples, the oxidation time to $^{18}O_2$ was the same, 4 min. Again, one can see that the leading edge position of the peaks shows that both isotopes are on the surface after oxidation. This is true for all three oxidation events. After $^{16}O_2$ oxidation for 1 h [Fig. 5(a)], both peaks have similar widths with $^{18}O$ being somewhat broader [$\Delta_{1/2}(^{16}O) = 0.54$ keV, $\Delta_{1/2}(^{18}O) = 0.73$ keV], again indicative of similar depth distributions for both isotopes. Additional $^{16}O_2$ oxidation for 4 h [Fig. 5(b)] results in both peaks broadening [$\Delta_{1/2}(^{16}O) = 0.75$ keV and $\Delta_{1/2}(^{18}O) = 0.92$ keV]. Both peaks become broader, which suggests that this layer contains a mixture of both isotopes (although not necessarily uniform), which we describe by the phrase "isotopic mixing." As the oxidation develops even further [Fig. 5(c)], we observe that $\Delta_{1/2}$ for $^{16}O$ (1.16 keV) becomes greater than for $^{18}O$ (0.84 keV). The latter is close to the $\Delta_{1/2}(^{18}O)$ value we observe after oxidation for 5 h [Fig. 5(b)]. This implies that we have a transition to a growth mechanism with oxide growth mainly at the interface. It is worthwhile to note that the peak width at the transition point increases with increasing temperature; $\Delta_{1/2}(^{18}O) \sim 0.60$ keV at 1120 K (Fig. 2) and $\Delta_{1/2}(^{18}O) \sim 0.92$ keV at 1170 K (Fig. 5). This is an indication that the oxide thickness for the isotopically mixed layer increases with temperature.

Isotopic mixing is also observed at lower temperatures. MEIS spectra for samples sequentially oxidized at 1020 K and $10^{-2}$ Torr are shown in Fig. 6. The presence of isotopic mixing at this temperature is deduced from the following observations: (i) both isotopes are located on the surface, as seen from the positions their leading edge, (ii) the peak widths are similar, and (iii) both peaks broaden as the oxidation proceeds [Figs. 6(a) and 6(b)]. Similar to the previous samples, $\Delta_{1/2}(^{16}O)$ is slightly smaller than $\Delta_{1/2}(^{18}O)$, reflecting nonuniform mixing. The kinetics of silicon oxidation at this temperature and pressure are very slow. For this reason, we have not reached the transition point to nonmixing behavior within the $\sim 44$ h of oxidation time shown in Fig. 6(b).

Isotope profiles of the samples oxidized at 1020 (Fig. 6), 1120 (Fig. 2), and 1170 K (Fig. 5) are shown in Figs. 7, 8, and 9, respectively. The procedure of energy spectra simulation employed to calculate the profiles is described in the Appendix. The profiles are normalized in such a way that the total oxygen density near the oxide surface equals 1. Several features of these profiles should be pointed out.

(i) Our simulation shows that for very thin oxides, both isotopes are distributed throughout the film [Figs. 7(a), 7(b), 8(a), 9(a), and 9(b)].

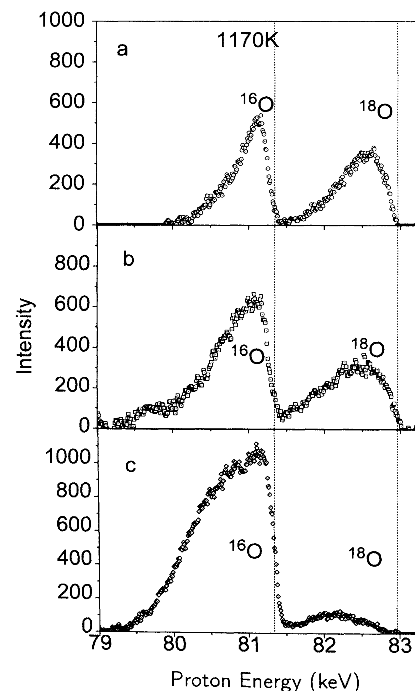


FIG. 5. The evolution of the MEIS spectra with reoxidation in $^{16}O_2$ at 1170 K and oxygen pressure of about $10^{-2}$ Torr. All three samples were first oxidized in $^{18}O_2$ at 1170 K and $10^{-2}$ Torr for 4 min. Subsequent oxidation times in $^{16}O_2$ were (a) 60 min, (b) 300 min, and (c) 1860 min. Dashed lines indicate the leading edge positions for both isotopes calculated with the binary collision model.

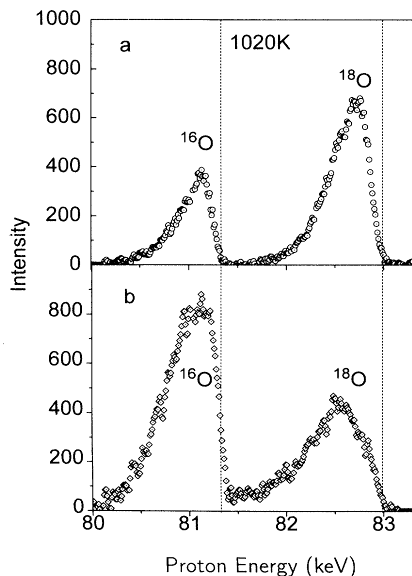


FIG. 6. MEIS spectra for Si(100) samples oxidized at 1020 K and $10^{-2}$ Torr. Exposures in $^{18}O_2$ were 10 min for both samples. This first oxidation step is followed by oxidation in $^{16}O_2$ for (a) 165 min and (b) 2640 min.

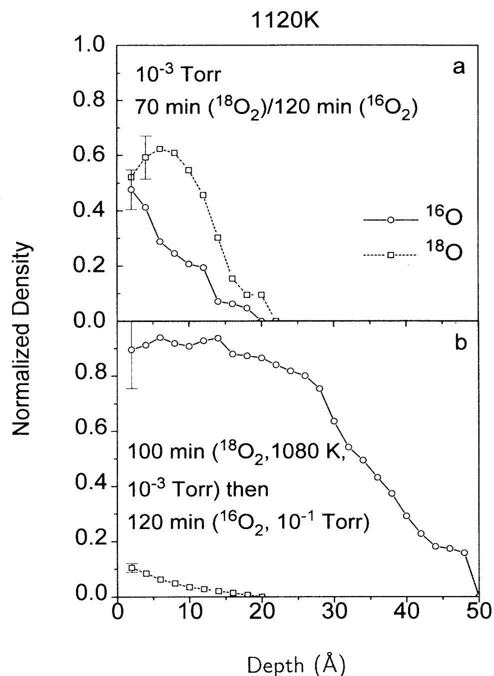


FIG. 8. Isotopic depth distributions for the sample oxidized at 1120 K. The original MEIS spectra are shown in Fig. 2.

(ii) The isotope depth distributions are *not* uniform, as a simple visual analysis of the MEIS peak shape of the thinnest films implies. The net concentration of both isotopes decreases as we approach the interface; this seems to be a characteristic of the transition region discussed in detail below. However, for the cases we present, the $^{18}$O density first increases just below the surface and later decreases, whereas the $^{16}$O concentration decreases steadily from the surface into the film. The location of the maximum in the $^{18}$O concentration depends on the oxidation time in $^{16}O_2$ (or the final oxide thickness): It moves away from the surface and its maximum value decreases as the oxidation develops further [cf. Figs. 7(a) and 7(b); Figs.

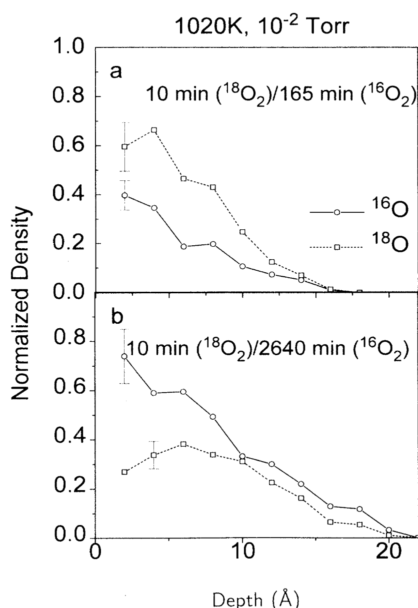


FIG. 7. Isotopic depth distributions for the sample oxidized at 1020 K. The original MEIS spectra are shown in Fig. 6. Data points (circles for $^{16}$O and squares for $^{18}$O) are deduced from spectral simulation, as explained in the Appendix.

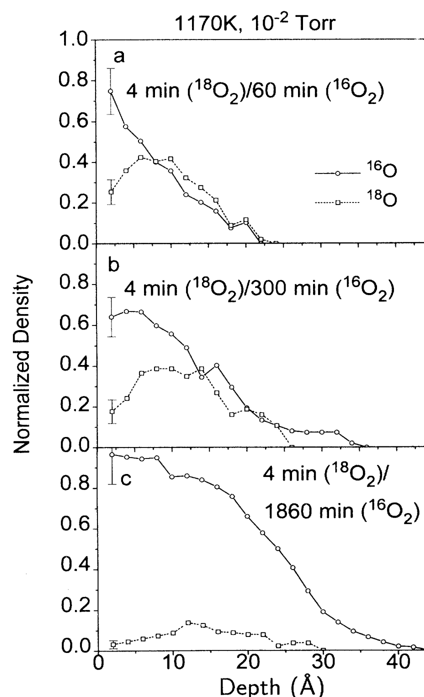


FIG. 9. Isotopic depth distributions for the sample oxidized at 1170 K. The original MEIS spectra are shown in Fig. 5.

9(a) and 9(b)].

(iii) For thicker ~40–50-Å films [grown by reoxidation in $^{16}O_2$ with a 13–15-Å starting $Si^{18}O_2$ film, see Figs. 8(b) and 8(c)], the $^{18}O$ is not distributed throughout the film, but is concentrated near the outer surface. This implies that the oxide grows via $^{16}O$ reaction with Si at or near the interface with an isotopically mixed layer remaining near the surface. The dynamics of this process can be observed on the sample oxidized at 1170 K (Fig. 8), where all three samples were initially prepared under the same oxidation conditions in $^{18}O_2$ and, therefore, have similar thickness after the first oxidation step. After a 60-min reoxidation in $^{16}O_2$, both isotopes have the same thickness (~20 Å) [Fig. 9(a)]. Additional exposure in oxygen (5 h) results in an oxide thickness of ~34 Å, with the thickness of the $^{18}O$ containing region of about 24 Å [Fig. 9(b)]. As the total oxide film gets thicker, ~40 Å [Fig. 9(c)], the thickness of the $^{18}O$ containing layer grows more slowly, ~28 Å. The point where a transition to nonmixing behavior occurs depends on the temperature, with higher values for higher temperatures [Fig. 8(b) and Fig. 9(c)].

(iv) Concomitant to the interface reactions, an isotopically mixed region develops at the surface of the thicker oxides, and the overall amount of $^{18}O$ in the film decreases with the oxidation time. (A more complete study of the surface "exchange" reactions will be reported elsewhere.[78] In particular, we found that the "exchange" reaction is enhanced by transition-metal impurities on the oxide surface.)

Finally, while we present results only for 115° scattering angle, we have performed this analysis for four different scattering angles (115°, 119°, 125°, and 132°). The profiles deduced from different angles are very similar. This fact indirectly supports our assumption of oxide film homogeneity. If the oxide thickness variation was significant or if laterally separate $Si^{18}O_2$ and $Si^{16}O_2$ regions were formed, one would expect different profiles for different scattering angles (especially for the variation on the vacuum-$SiO_2$ side of the film, as ions that travel in $SiO_2$ suffer a large inelastic energy loss and those that travel in vacuum do not). However, the limited angular range precludes good quantitative measurements on how flat the $Si/SiO_2$ interface is.

High-energy ion beams (especially of heavy ions) at high ion dose may cause ion induced mixing at the interface between two materials.[84] To make sure that the mixing we observe is not caused by the proton beam, we have performed data acquisition on one sample with a very low proton beam exposure ($\sim 5\times 10^{15}$ protons $cm^{-2}$). According to the estimates in Sec. II, this dose corresponds to the displacement of less than 1% of the atoms. The MEIS spectrum taken under this low-dose condition also shows isotopic mixing and is very similar (but with poorer statistics) to those taken at our typical dose of $\sim 3\times 10^{16}$ protons $cm^{-2}$. This is clear evidence that the depth distributions observed in our experiments are a result of the oxidation reaction rather than of proton-solid interactions.

One result is that we also observe oxygen loss during oxide growth at high temperatures. The area under the $^{18}O$ peak is proportional to the integrated amount of this isotope in the film, and becomes smaller with continuing oxidation in $^{16}O_2$ (Fig. 5). This implies that some of the initially adsorbed $^{18}O$ leaves the film during subsequent oxidation, and that the loss increases with oxidation time. Another observation illustrating oxygen loss comes from comparing XPS and MEIS data. For the sample used in Fig. 2(b), the oxide thickness was also determined by XPS. After oxidation in $^{18}O_2$, this XPS thickness is 13 Å [Fig. 4(a)], and after reoxidation in $^{16}O_2$ it is about 50 Å [Fig. 4(c)]. Therefore, a 0.26:1.0 $^{18}O$ to $^{16}O$ ratio should have been expected provided that no $^{18}O$ left the film during oxidation. However, if we compare peak areas in MEIS [Fig. 2(b)], we obtain a ratio of about 0.04:1. Therefore, much of the initially absorbed $^{18}O$ must be leaving the film under these conditions.

An important problem is stoichiometry and concentration gradients in the thin oxide film. Oxygen and silicon backscattering spectra for a 50-Å oxide film grown at IBM facilities and corresponding oxygen and silicon profiles are depicted in Figs. 10 and 11, respectively. Our simulation procedure demonstrates an oxygen to silicon ratio of approximately 2.0:1 in the film (Fig. 11), as expected from the known $SiO_2$ stoichiometry. There is, however, a transition region between $SiO_2$ and crystalline silicon where the oxygen concentration (and the O/Si ratio) is lower. This transition region is variously ascribed in the literature to compositional changes,[16,85,86] interface roughness,[87,88] stressed oxide layers[9] or other structural inhomogeneities in the near interfacial oxide. The silicon concentration increases in the transition region when

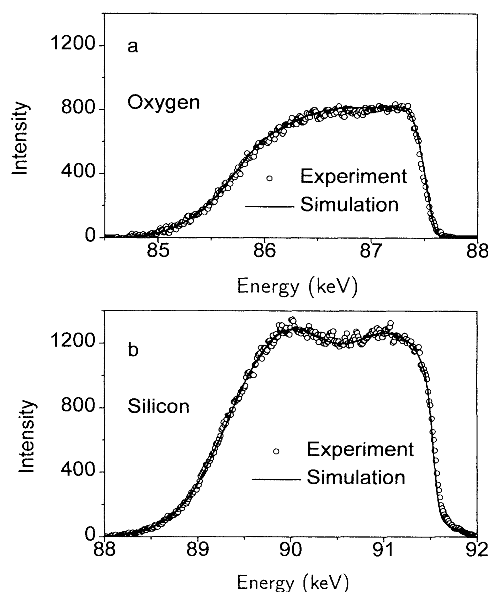


FIG. 10. (a) Oxygen and (b) silicon energy spectra for high-quality 50-Å oxide grown at 1070 K. The incidence beam was aligned along ($\bar{1}\bar{1}0$) direction. The scattering angle is 80°. Open circles are experimental data; solid lines show the best fit with our simulation procedure (see the text and the Appendix).

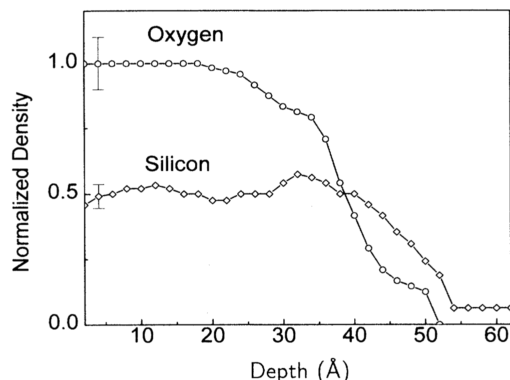


FIG. 11. Oxygen (shown as circles) and silicon (diamonds) depth distribution as a function of the distance from the oxide-vacuum interface derived from the data in Fig. 10. The densities are normalized with respect to the oxygen density in "bulk" silicon near the oxide surface. Several Å of substrate Si is also visible due to thermal vibration and distortion by the oxide layer.

compared to the "bulk" $SiO_2$ near the oxide surface. Because the backscattering yield in the channeling geometry used in Fig. 11 may be lower due to shadowing, we have performed measurements on the same sample in a random incidence geometry [Fig. 12(a)]. The silicon concentration profile corresponding to this spectrum [Fig. 12(b)] shows that the silicon concentration in the "bulk" oxide is $2.1\pm0.1$ times lower than in crystalline silicon and that the silicon concentration in the transition region gradually increases to the value of crystalline silicon. One should keep in mind that this "transition region" refers to the near-interfacial region with different composition and structural properties from bulk Si or $SiO_2$, and does not necessarily coincide with the isotopically mixed layer resulting from the oxidation, which can become buried in the growing films (see below). The existence of the transition region is also supported by our XPS experiments (Fig. 13), where intermediate oxidation states are seen in the Si $2p$ photoelectron spectrum between the substrate peak ($Si^0$) and the peak corresponding to $SiO_2$ ($Si^{4+}$). This suggests the presence of some incompletely oxidized Si.

From our MEIS experiments (for the given energy loss and straggling parameters, see the Appendix), we estimate the thickness of the transition region for this sample to be $15\pm4$ Å [Fig. 12(b)]. This value is within the range reported in the literature (5–30 Å).[11,12,14,16,17,37,38,40] The thickness of the transition region depends strongly on the probing techniques; even the definition of the transition region varies from one study to another. For instance, from ellipsometry measurements, the transition region is understood as a layer with optical properties different from both bulk oxide and crystalline silicon.[89,90] Simulation of ellipsometry energy and angular spectra taken on the same sample with the MEIS gives the best fit if the transition region is about 6 Å.[91] We will discuss reasons for the discrepancy of the determination of the thickness of the transition region and stoichiometric oxide film with MEIS, ellipsometry, and XPS elsewhere.[91] Photoemission studies consider the transition region as a layer with local electronic configurations different from ideal $SiO_2$. The effect of electronic configuration on the

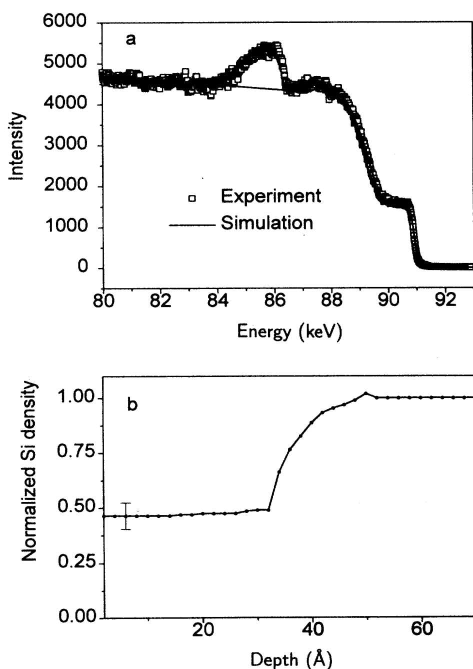


FIG. 12. (a) MEIS spectrum for a 50-Å oxide taken under random scattering conditions, and (b) the corresponding silicon depth distribution up to 70 Å. The scattering angle is ~86°. The experimental data are shown by open squares; the solid line shows the result of the silicon depth distribution simulation. The oxygen peak at ~85–86 keV [shown also in Fig. 10(a)] was not considered in the simulation. The silicon density (b) is normalized to the value in the crystalline silicon.

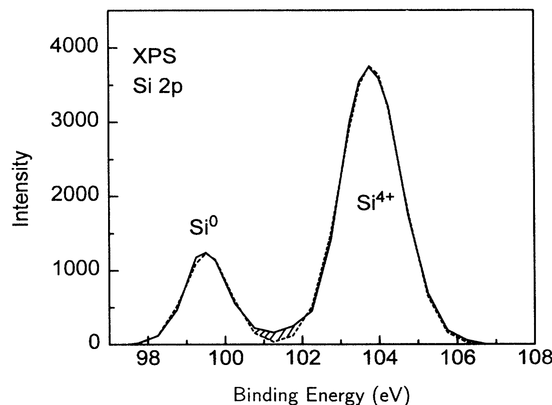


FIG. 13. XPS spectrum for the 50-Å oxide. The solid line shows the experimental data; the dashed line represents a fitting using two Gaussian lines corresponding to $Si^{4+}$ and substrate atoms ($Si^0$). The shadowed area, formed by suboxide states, is still visible in this 50-Å film, although it is clearer for thinner films.

MEIS results is negligible. We use the term transition region to mean a layer of different composition from pure Si and $SiO_2$. One should mention that our MEIS estimate of the thickness of the transition region is influenced by the energy loss and straggling parameters.

## IV. DISCUSSION

Before discussing the mechanism(s) of silicon oxide growth during the initial oxidation, we summarize our main experimental observations.

(i) For ultrathin films, we observe overlapping depth profiles for both oxygen isotopes during the first 20–25 Å of oxide growth, despite the fact that the samples were exposed sequentially to these isotopes. The isotopic mixing holds for all temperatures and pressures used in our experiments.

(ii) The isotopic mixing behavior changes as a function of thickness. The mixing happens throughout the film for ultrathin film growth. For thicker final oxide films, two isotopically different regions are observed; for thicker initial oxide films,[78] the two isotopically mixed regions are separated, one at the surface, another at the interface.

(iii) Some of the initial isotope used to oxidize is lost during subsequent oxidation.

(iv) There is a thin transition region between crystalline silicon and silicon dioxide. The silicon density in the transition region is higher than in the "bulk" oxide, while the oxygen density is lower.

### A. Breakdown of the phenomenological models for silicon oxidation in the limit of ultrathin films

We now address the isotope profiles in the context of the reactive layer[12,23] and Deal-Grove models,[19] and examine the applicability of each model during the initial stage of silicon oxidation. The reactive layer model proposes two stages for the initial oxidation. In the first stage, a reactive layer is formed with silicon diffusion through the growing layer to the outermost oxide surface, followed by reaction with oxygen at the surface. After this layer is formed, a second stage begins in which oxidation occurs on top of this reactive layer with both oxygen and silicon diffusion to the top of the layer ($O_2$ through the bulk $SiO_2$ and Si through the reactive layer). The thicknesses of our 15–20-Å oxides [Figs. 7, 8(a), and 9(a)] are of the same order as the reactive layer proposed in this model.[23] Therefore, for these films, the reaction should take place on top of the reactive layer, which in this case is at the oxide surface. Thus after an $^{18}O_2$, then $^{16}O_2$, sequential oxidation we should expect an $^{18}O$ oxide layer near the interface and an $^{16}O$-containing oxide on the surface. This behavior is not consistent with our 13–15-Å initial oxide results (Figs. 7–9), which show both isotopes distributed throughout the oxide film.

If the Deal-Grove model were applicable (Fig. 1), on the other hand, a reverse isotopic ordering (with $^{18}O$ at the surface and $^{16}O$ near the interface) would be observed. Our data for very thin oxide films [Figs. 7, 8(a), and 9(a)] clearly contradict this. The correct model must account for similar depth distributions for both isotopes for thin films (15–20 Å).

For the 50-Å oxides with a 13–15-Å initial $Si^{18}O_2$ layer, the reactive layer model predicts an oxygen profile that has a different ordering ($^{16}O$ at the surface and $^{18}O$ near the interface) than our MEIS spectra show [Fig. 8(b)]. The profile characteristic of the Deal-Grove model (with separate $^{18}O$ and $^{16}O$ regions) also does not agree with the experimental data [Fig. 8(b)]. However, if we ignore the surface exchange reaction, the basic ideas of the Deal-Grove model (oxygen diffusion through the oxide and reaction at or near the interface) are closer to our data than the reactive layer model. The $^{16}O$ concentration is very high at the interface of our 40–50-Å films, as predicted by the Deal-Grove model; one major inconsistency, however, is that the Deal-Grove model does not predict behavior that could result in isotopic mixing near the oxide surface for 40–50-Å oxides.

The applicability of the Deal-Grove model to thin films is still under discussion,[12,20] as noted above. Several groups have explored oxidation kinetics for thin ( < 100-Å) oxide films and found that they differ from Deal-Grove kinetics.[6,8,9,11,12,22,24] It has been suggested recently that this deviation could be caused by an error in the oxide thickness determination, and it was claimed that the Deal-Grove model was relevant for very thin films as well.[92,93] In contrast to these kinetic studies, our experiments show an atomistic "cross section" of the initial oxidation-oxygen isotope distributions in the growing film, which show the location of the reaction and diffusion pathways; they thus provide direct evidence that the Deal-Grove model cannot be used for very thin ( ~ 15–25-Å) oxides. For the same reason, models[22] that explain the fast oxidation kinetics for very thin oxides by modifying the interfacial reaction or oxygen diffusivity, while still working within the Deal-Grove construct, are not consistent with our results.

Recent results on the initial oxidation of silicon at room temperature[94–97] showed inverse-logarithmic kinetics and were interpreted as implying a field-assisted oxidation (Cabrera-Mott) mechanism.[1,6] According to this model, usually used to explain the initial oxidation of metals, the oxidation reaction takes place either at the oxide/vacuum or oxide/substrate interface depending on the nature of diffusing species. The reaction is enhanced by an electric field, which is developed through the oxide film during the oxidation. Although our results cannot rule out this mechanism for the growth of the first oxide layers and room-temperature oxidation, the isotope profiles clearly show that the Cabrera-Mott model (with reaction at either of the interfaces) is not responsible for the high-temperature oxidation of the oxide films thicker than 15 Å.

### B. Mechanisms of oxide film growth during the initial oxidation

Our data show that sequential isotopic oxygen exposures for ultrathin oxide layers results in the formation of a thin ( ~ 15–20 Å) layer in which both isotopes have a similar depth distribution [Fig. 14(a)]. After the forma-

tion of this layer, two reaction pathways develop. The first involves oxygen diffusion through the oxide reacting with silicon at and/or near the interface, and is responsible for the film growth, leaving a mixed isotope distribution at the surface of the oxide [Fig. 14(b)]. The second is a reaction at the surface that results in an exchange of one isotope for the other with no net change in Si to O stoichiometry.

There are several possibilities to explain the similar depth distributions of the two isotopes for thin oxides: (1) lateral inhomogeneities, such as oxide island growth; and (2) isotopic mixing during the initial oxidation. Isotopic mixing, in turn, may be caused by several mechanisms: (i) Oxygen reaction with incompletely oxidized silicon throughout the transition oxide region. (The incompletely oxidized silicon in the near interfacial oxide could be silicon suboxides, or silicon interstitials and/or clusters in the oxide.) (ii) Atomic oxygen diffusion within the oxide, perhaps via an exchange mechanism.

As noted above, growth mode issues (layer vs island growth) are still unresolved. Much of the work on this subject has used photoemission methods.[14,28–30,35,98–100] Some experiments reveal a stepwise increase in the thickness of the oxide or suboxide states on Si(100).[30,98,99] Similarly, an oscillatory behavior of the $Si^{1+}$ and $Si^{3+}$ intensities on Si(111) has been interpreted as evidence for layer-by-layer growth.[101] On the other hand, some authors also claimed (based on XPS results) that 3D island growth does take place under certain oxidation conditions.[28,29,101] Engel and co-workers[29] have presented results that imply layer-by-layer growth only at temperatures less than 900 K; whereas at higher temperatures, the initial oxidation is 3D, involving nucleation and growth of bulklike oxide islands. Contrary to this, other XPS experiments[28,101] were interpreted in terms of nonuniform oxidation (in the vertical direction) at 573 K, and as layer-by-layer growth at higher temperatures, 873–1073 K.

Using HRTEM, Gibson and co-workers[31–34] observed that steps on the Si(111) surface were immobile during oxide film growth, indicative of layer-by-layer growth. Cross-sectional HRTEM does not demonstrate oxide film inhomogeneity characteristic of 3D island growth;[24,44,102] actually the $Si/SiO_2$ interface is observed to be very abrupt.[11] These observations argue against the 3D island growth model as the main source of the similar depth distribution of oxygen isotopes observed for very thin films. We also note that in-air atomic force microscopy (AFM) experiments performed in our laboratory and elsewhere on thin oxides do not show high variations in surface morphology, as would be expected for island growth.[103–106] However, the AFM image resolution is limited by tip shape and size effects;[107] thus, if the surface islands are smaller than the AFM tip radius (typically several hundreds of Å), the real surface morphology may be hidden.

If lateral inhomogeneities were to explain the overlapping oxygen isotope depth distributions in our MEIS spectra, one would need to assume that a considerable portion of the surface is clean Si (or, at most, very slightly oxidized) after oxidation in $^{18}O$. Since the average thickness of the oxide layer is $\sim 10–15$ Å at this point, this implies that the oxide island or layer thickness was even thicker in some places and close to 0 Å in other places during the initial oxidation. This is inconsistent with our results (Sec. III) and most literature results. The broadening of the $^{18}O$ distribution during reoxidation in the $^{16}O_2$ environment also cannot be explained by lateral inhomogeneities. Therefore, lateral inhomogeneity during the initial oxidation is unlikely to be the dominant reason for the similar depth profiles observed for the oxygen isotopes. We favor a model in which the isotope profile overlap is caused by *oxidation of incompletely oxidized silicon in the transition region.* However, our results determine neither the configuration of the incompletely oxidized silicon nor the mechanism of its formation.

Assuming that incompletely oxidized silicon exists in the near-interfacial region, then switching exposures from one isotope to another could easily lead to isotope profile overlap in the suboxide region, as we observe. We thus argue that we have both interfacial (in an analogy to the Deal-Grove model) and near-interfacial reactions

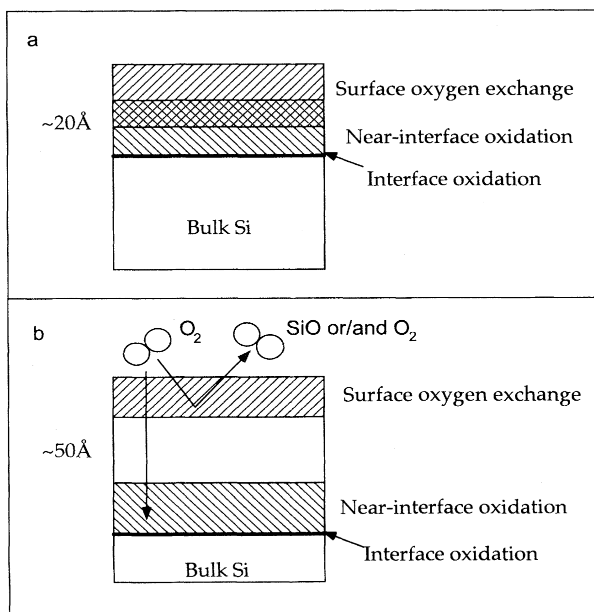


FIG. 14. Schematic model for silicon oxidation. Oxygen atoms may either react at (i) the interface (and possibly provide the interstitial Si atoms/clusters into the transition region), (ii) react with Si in the form of interstitial atoms/clusters or suboxides in the transition layer (near-interfacial reaction), or (iii) exchange with other oxygen atoms at/near the oxide surface. (a) At the earliest stage of oxidation (15–25-Å oxide), the near-interface transition region starts from the surface, and as a result, the (near-interfacial reaction and the surface reaction overlap. (b) For thicker films, oxygen will diffuse through the completed $SiO_2$ layer and react at the interface or in the near-interface transition region. This will leave behind a mixed layer at the surface in our case. Concurrently, the surface reaction still takes place (see the text).

during oxidation of the 15-Å initial oxide films. The interfacial reaction forms silicon oxide at the interface, and it continuously supplies the near-interfacial region with a substoichiometric oxide, interstitial silicon and/or silicon clusters. Recent spectroscopic ellipsometry measurements of a 100-Å silicon oxide were interpreted as offering evidence for a thin ($\sim$20-Å) mixed ($SiO_2$ + amorphous silicon) oxide layer near the interface.[90] Scanning-transmission electron microscopy–electron-energy-loss spectroscopy experiments also support the idea of silicon clusters in the thin oxide within about 10 Å from the interface.[85,86] Unoxidized Si atoms were directly observed recently during oxidation of four silicon layers grown by molecular-beam epitaxy on Ge(100).[108] Moreover, this study shows Ge/Si mixing in the transition region after the oxidation, the mechanism of this mixing may be similar to the mechanism of isotopic mixing suggested in our paper.

A suboxide is also seen in photoemission. The concentration of the suboxide states [$\sim$1–2 ML (Refs. 16 and 17)] does not seem to be high enough to give rise to the isotopic mixing in the whole (15–25 Å) film. However, if the suboxide states were constantly being regenerated, a 15–25 Å isotopically mixed film could result. Furthermore, the original classification of the $Si^{n+}$ suboxide states came from photoemission experiments where different chemical shifts were observed in the Si 2*p* photoelectron spectra; they were attributed to a Si atom with *n* oxygen bonds in the first coordination sphere.[16,17,25] It was shown that $Si^{1+}$ and $Si^{2+}$ states are localized within 6–10 Å near the interface, while $Si^{3+}$ suboxide spreads over about 10–30 Å from the interface.[16,25] However, recent experiments showed that the local electronic configuration in the second coordination sphere also contributes to the spectra,[42,109] implying that the "traditional" XPS analysis may have some limitations in identifying the nature and quantity[43,110] of incompletely oxidized silicon. On the other hand, one should also mention that recent first-principle calculations support the original interpretation of the $Si^{n+}$ states.[111]

Provided that the rate of the near-interfacial reaction is proportional to the concentration of the incompletely oxidized silicon and recognizing that the concentration of suboxide states should be proportional to the amount of silicon over and above the "bulk-"oxide concentration [Fig. 12(b)], we find the reaction rate should increase throughout the transition region from zero in the bulk oxide to its limiting value at the interface. Actually, the reaction rate should be proportional to both the concentration of the suboxide and of the dissolved $O_2$ that diffuses in from the surface. These two should have opposite gradients in the transition region; thus, the reaction may take place throughout the transition region. Although we cannot define the exact thickness of the near interface region where the oxidation takes place, nor the concentration gradients and relative reaction rates (they probably depend on the oxidation conditions), the general idea of an interface plus near-interface reaction is perhaps the most straightforward way to understand our results (see Fig. 14).

Concerning the surface reaction, we observed $^{18}O$ loss from the surface when reoxidizing in $^{16}O$. This suggests a dynamic exchange process occurring close to the oxide-gas interface in which $^{16}O$ incorporates, while $^{18}O$ is lost from the surface, either in the form of $Si^{18}O$ or $O_2$. While we do not observe the desorbing species directly, SiO desorption is known to take place at the temperatures explored in our experiments.[14,51,54,112,113] Mass-spectrometry experiments under UHV conditions show that molecular oxygen does not desorb from a silicon surface up to 1400 K,[113] although an $O_2$ isotopic exchange surface reaction cannot be ruled out at the high pressures used during the oxidation. The increased concentration of $^{18}O$ just below the surface with oxide depth, and the increase in the depth at which the transition to a negative $^{18}O$ gradient occurs with increasing oxidation time [Figs. 7, 8(a), 9(a), 9(b)], can also be explained by either $O_2$ exchange or $Si^{18}O$ desorption from the oxide surface.

We believe that an "interfacial+near-interfacial+surface reaction" model is more consistent with our experimental results than "simple" interfacial reaction models, such as the Deal-Grove model. A key point of any correct model should be the active role of the transition region in the initial oxidation, particularly in the reoxidation of incompletely oxidized silicon. The reactive layer model also proposes a transition (reactive) layer. In contrast to the reactive layer model where oxidation takes place on top of the reactive layer, our results suggest a more homogeneous reaction rate *throughout* the transition region. It is also possible to explain the seemingly contradictory observations of layer-by-layer growth (as seen by others) and isotopic mixing. Within an interface+near interface reaction model, layer-by-layer growth would result from the interfacial reaction, while isotopic mixing would be caused by the near-interfacial reactions.

It is unclear if a transition to a pure interfacial reaction takes place with increasing oxide thickness or if the near-interfacial reaction continues for the thicker films. If the second, near-interfacial channel for oxide formation increases relative to the interfacial channel (in relative rates) as the film becomes thinner, then this could explain the faster oxidation kinetics for very thin oxide films, a departure point of phenomenological modifications of the Deal-Grove model for thin films. Our experiments starting with thin (10–15 Å) $Si^{18}O_2$ films reoxidized in $^{16}O_2$ show a transition to Deal-Grove-like behavior for 40–50-Å oxides [Figs. 8(b), 9(c)]. This does support the idea that oxygen diffuses to the interface and that the oxidation reaction does not proceed uniformly in thicker films. However, it is still possible that the reaction occurs throughout the thin (10–15 Å) transition region near the interface and that the near-interfacial channel continues to be important for the thick films, where the Deal-Grove model is traditionally used to describe the oxidation kinetics.

A more speculative problem concerns how the incompletely oxidized silicon is generated. It can result from (i) a simple partial oxidation at/near the interface, or (ii) silicon generation or injection in the oxide, concepts which have appeared in some of the recent literature.[47–49,114,115] The basic idea in the second case is that Si is injected into

the oxide (and Si substrate) during the reaction at the interface. The rate of Si generation is thought to be about one silicon interstitial formed for each silicon atom oxidized.[114] Indirect evidence for this comes from stacking faults seen in the substrate Si after oxidation.[24,114,116] Other related evidence comes from HRTEM experiments on Si(111) (Ref. 31) and STM experiments on Si(100),[117–119] showing that silicon atom generation occurs during oxygen interaction with silicon surfaces at submonolayer coverages and, as a result, silicon clusters appear on the surface.

Some authors who have proposed the "interstitial Si generation" model consider the possibility that silicon oxidation occurs as a reactive transformation from crystalline silicon to crystalline $SiO_2$ (cristobalite) plus interstitial silicon at the interface. Tiller[47] suggested that there is a thin ordered oxide layer near the $SiO_2$/Si(100) interface that plays an important role in oxidation and can help in understanding the nature of electrical defects at the interface and in the near interfacial oxide. Within this model, subsequent oxidation of the interstitials destroys this crystalline oxide phase at its junction with amorphous $SiO_2$ and generates new vitreous silica, while newly formed crystalline oxide at the interface with the Si-substrate pushes the oxidation further into the bulk. However, the possible existence of a crystalline oxide near the interface is also a matter of intense debate.[14,33,88] Several groups have claimed their results showed evidence for an ordered oxide near the interface,[24,44,45,120–122] while other investigators[33,88] do *not* observe a crystalline oxide using the same techniques.

The speculation[47] about interstitial Si generation (and diffusion into the oxide) to explain the excess Si in the oxide is neither experimentally proven nor completely satisfying. How deep into the oxide are the Si interstitials injected? What fraction of the oxide is formed via the interfacial channel and what fraction is formed via the oxidation of interstitials? Why is the thickness of the isotopically mixed layer for some of our samples [e.g., Figs. 7(b), 8(b), and 9(a)] twice that of the oxide thickness after the first step of the oxidation in $^{18}O_2$ ($\sim 13$ Å)? Even in a marginal case, when all generated silicon atoms diffuse into the oxide, one should expect only $^{16}O$-oxide near the interface for these oxides. However, this is not what we observe, implying that other sources may contribute to the isotopic mixing. An additional source of isotopic mixing may involve atomic oxygen exchange diffusion via oxide defects, as suggested by Mott and co-workers.[12]

An important unresolved issue is to understand how the surface exchange happens (whether through SiO desorption or $O_2$ exchange) and its dependence on $T$, $p$, and film thickness. It would be interesting if SiO desorbs on the oxidation part of the $(p,T)$ phase diagram. The traditional viewpoint[14,50,51] is that the high-pressure low-temperature part of the $(p,T)$ diagram is characteristic of oxide formation, whereas SiO desorption and surface etching occurs only on the other, low-pressure high-temperature side. SiO desorption during initial oxidation was also observed recently by Ono, Tabe, and Kageshima[123] and oxygen loss was found by NRA during initial silicon oxidation.[66] SiO desorption may contribute to isotopic mixing near the surface. SiO desorption from a stoichiometric $SiO_2$ surface should leave an excess of O at the surface. This could then diffuse below the surface and contribute to isotopic mixing in the near-surface regime. On the other hand, $O_2$ dynamic isotope exchange reactions may become important at very high pressures, although they would not be observed in UHV experiments. In either case for ultrathin films, the near-interfacial reaction and the near-surface dynamic exchange would be occurring in the same place, while for thicker films these two processes would be distinct (Fig. 14).

An important practical issue concerns the extent that these results and models are relevant for gate oxides grown under realistic processing conditions. RCA cleaning and its various modifications (wet chemistry methods) are proven to be very effective in contamination removal (metal, hydrocarbons, etc.) and surface smoothing.[124–126] For our *in situ* oxidation, we have used a more traditional surface science approach, i.e., sample degassing and protective oxide desorption under UHV conditions. To avoid contamination, we minimize the chamber pressure; however, we cannot guarantee the absence of impurities in amounts below the MEIS sensitivity. Oxidation in stainless steel UHV chambers is known to introduce more impurities than state-of-the-art quartz furnaces. We also only demonstrate that isotopic mixing holds in the $T=1020-1170$-K range for the oxygen pressures in the $10^{-1}-10^{-3}$-Torr range, several orders of magnitude lower than the $\sim 1$ atm used in state-of-the-art device manufacturing. However, our results are consistent, in general, with the results of other isotope labeling experiments in which the oxidation of thin[24] and thick[68] films were performed at much higher pressures in quartz furnaces.

## V. CONCLUSIONS

We have studied the growth mechanism of ultrathin silicon oxide films, using high-resolution ion scattering with $^{18}O_2/^{16}O_2$ sequential oxidation. We find that neither the Deal-Grove model and its modifications, nor the reactive layer model, offer an accurate description of the behavior of very thin ($<50$ Å) films. According to our results, oxide films containing a mixture of both oxygen isotopes are formed during the initial stages ($<25$ Å) of thermal oxidation. The mixing is caused by oxygen reaction with incompletely oxidized silicon throughout the transition region. This is followed by oxygen diffusion through previously formed oxide layers to the interface and oxide formation at and near the interface. We also observe oxygen loss from the surface, suggesting SiO desorption or an $O_2$ surface exchange reaction. Contrary to the traditional viewpoint, this oxygen loss takes place during oxide film growth, on the "oxidation part" of the $(p,T)$ phase diagram.

## ACKNOWLEDGMENTS

The authors would like to thank Dr. D. Buchanan (IBM) for his advice and for providing a high-quality ox-

ide sample. We would also like to thank Dr. R. A. Bartynski, Dr. D. Hensley, Dr. V. A. Yakovlev, Dr. P. Statiris, Dr. Y. Wu, Dr. A. Diebold, and Dr. J. Mayer for their help and comments. This work was supported in part by the National Science Foundation (DMR-9408578) and the Petroleum Research Fund (28788-AC5). E.P.G. acknowledges partial support from the CAST/NAS program.

## APPENDIX: HIGH-RESOLUTION DEPTH PROFILING WITH MEIS

As mentioned in Secs. II and III, while it is possible to qualitatively distinguish different oxidation modes from a simple examination of the MEIS peak shapes (Fig. 1), we can get more detailed information about the isotope concentration and depth distribution in the film through simulations. To simulate an energy spectrum, we model the sample as a uniform film with a series of thin slabs parallel to the surface. The scattering yield, $Y_{ij}$, from the $i$th element in the $j$th slab is given by

$$Y_{ij}=T\sigma_i(E,M_i,Z_i)n_{ij}\Delta x \ , \tag{A1}$$

where $\sigma_i(E,M_i,Z_i)$ is the scattering cross section for the $i$th element in each slab. $\sigma_i$ depends on the incident energy $E$, mass ($M_i$), and charge ($Z_i$) of that element, $n_{ij}$ is the concentration of the $i$th element in the $j$th slab, $\Delta x$ is the slab thickness, and $T$ is a normalization factor (that also includes the proton beam dose). We use cross sections calculated using a Molière interatomic potential for the proton-target atom interaction.[127] Since silicon oxide film grown on silicon substrate is thought to be mostly amorphous and we are mainly concerned with the oxygen yield, channeling, dechanneling, and blocking effects are ignored.

Since protons scattered below the surface lose their energy during both the incoming and the outgoing trajectories, the energy peaks from each slab are shifted relative to each other proportional to the value of the energy loss per unit path length (the electronic stopping power, $dE/dx$).[55,56,128] We choose each slab thin enough (2 Å) to neglect the energy loss changes within the slab, for both the inward and outward paths (the surface energy approximation[128]). The electronic stopping power in silicon oxide is not known and has, therefore, to be calculated. There are several approximations in the literature that give slightly different values.[129] In our calculations, we use the Andersen-Ziegler values[73] that have proven to give reasonable values for a variety of systems. The electronic stopping power is energy dependent, with a maximum around 100 keV for protons interacting with oxygen and silicon. Thus, our choice of proton energy helps to increase the depth resolution. It is also worthwhile to note that the changes in stopping power with energy near the maximum are relatively small.[73] Therefore the electronic energy loss along the inward path, where the proton energy is about 100 keV, is close to the loss along the outward path, where the proton energy is in the 80–90-keV range. The Andersen-Ziegler approximation allows one to determine the electronic stopping power only for elemental targets. In order to consider compositional and density changes for $SiO_2$, we use Bragg's rule[128] $dE/dx=\sum_i(dE/dx)_i n_i/N$; $N=\sum_i n_i$. It should be mentioned that the stopping powers for silicon and oxygen (17.1 eV $cm^{-2}/10^{15}$ atoms for O, and 24.4 eV $cm^{-2}/10^{15}$ atoms for Si) (Ref. 73) are close to that of the electronic stopping power for 80–100 keV protons traveling through $SiO_2$ (14.6 eV/Å, in turn rather close to the stopping power in bulk Si, 12.2 eV/Å); therefore, the change in stopping power in the nonstoichiometric transition region should be relatively small.

Another important factor that affects the MEIS energy spectra is energy straggling; this reflects the broadening of the proton energy, due to the stochastic nature of energy losses by electronic excitations.[55,130–132] The total-energy peak broadening $\Omega^2=\Omega_0^2+(K_i\Omega_{\rm in})^2+\Omega_{\rm out}^2$ includes contributions from the instrumental resolution function ($\Omega_0$) and the straggling for the incoming and outgoing trajectories ($\Omega_{\rm in}$ and $\Omega_{\rm out}$, respectively; $K_i$ is the kinematic factor for the $i$th element). We include straggling in our simulation through a Gaussian energy distribution function, $F(E)$,

$$F(E)=(2\pi\Omega^2)^{-1/2}\exp[-(E-\langle E\rangle)^2/2\Omega^2] \ , \tag{A2}$$

where $\langle E\rangle$ is the mean (depth dependent) energy of the protons. Bohr's theory is usually used to calculate the straggling parameter, $\Omega$, in the limit of high ion energies.[133] For example, for oxygen and silicon Bohr's theory predicts $\Omega_B(\text{O})=32.3(x)^{1/2}$ (eV) and $\Omega_B(\text{Si})=42.7(x)^{1/2}$ (eV), where $X$ (Å) is the distance traveled in the sample. However, this free electron theory fails for slower ions (< 1 MeV for proton), in particular, for 100-keV protons. Therefore, we use the reduced straggling values given by the Lindhard-Scharff approximation:[130,134,135]

$$(\Omega_{\rm LH}/\Omega_B)^2\approx\begin{cases}L(y)/2 & (y<3)\ ,\\ 1 & (y>3)\ ,\end{cases} \tag{A3}$$

where $y=(v/v_0)^2/Z_2$, and $v_0$ is the Bohr velocity, $v$ is the proton velocity, and $l(y)=1.36y^{1/2}-0.016y^{3/2}$.[130,134,135] In particular, for 100-keV protons, this approximation results in reduced straggling compared to Bohr's expression with $L(y)/2$ values of 0.43 and 0.49 for silicon and oxygen, respectively. Finally, we use Bragg's rule to calculate the energy straggling parameter for $SiO_2$ from the known values for oxygen and silicon. The resulting straggling parameter is energy dependent, e.g., $20.4(x)^{1/2}$ eV for 100-keV protons and $17(x)^{1/2}$ eV for 80 keV with $x$ (in Å) the distance traveled in the sample. We take this energy dependence into consideration in our simulations. The final backscattering spectrum is obtained by integrating individual energy spectra from each slab. The only fitting parameters we use are the depth concentration of the oxygen isotopes and of the silicon atoms in the film.

In general, the above-mentioned approximations for electronic stopping power and energy straggling, and Bragg's rule for ion-solid interactions for compound materials, provide reasonable parameters for a wide variety of materials.[128,132] To make sure that the parameters are realistic, we cross-correlate MEIS depth profiles with XPS and ellipsometry results on the same sample.[91] For

this purpose, we use a high-quality gate oxide thermally grown in natural oxygen on Si(100) at an IBM fabrication facility. Ellipsometry gave a thickness of about 65 Å for this film,[91] whereas XPS yielded the ratio of $x/\lambda=1.7$ [see (1)], that corresponded to the oxide thickness of 51 Å (for $\lambda=30$ Å). Ellipsometry is known to overestimate silicon oxide thickness in the limit of ultrathin (<100 Å) films.[40,93] The MEIS energy spectra for oxygen and silicon taken in a channeling geometry are shown in Fig. 10. The dashed line shows the best fit using our stopping power and energy straggling parameters, and the silicon and oxygen depth distributions are shown in Fig. 11. The oxygen layer thickness from Fig. 11 is $50\pm4$ Å. The thickness of the silicon layers is about 56 Å; this results from the 50 Å of silicon atoms in the oxide and an additional 6 Å of substrate silicon visible to the proton beam in channeling. The data shown in Fig. 10 correspond to the scattering angle of about 80°. The profiles (Fig. 11) derived from the simulation of this set of data fit the spectra taken for this sample quite well at the scattering angle of 125°. This fact supports the validity of the simulation code, and shows that the film is rather uniform (otherwise, we should have observed an angular dependence for the energy spectra).


[1] N. Cabrera and N. F. Mott, Rep. Prog. Phys. **12**, 148 (1948).
[2] K. R. Lawless, Rep. Prog. Phys. **37**, 231 (1974).
[3] A. T. Fromhold, *Theory of Metal Oxidation. Volume I. Fundamentals. Defects In Cristalline Solids* (North-Holland, Amsterdam, 1976).
[4] P. H. Holloway, J. Vac. Sci. Technol. **18**, 653 (1981).
[5] K. Wandelt, Surf. Sci. Rep. **2**, 1 (1985).
[6] A. Atkinson, Rev. Mod. Phys. **57**, 437 (1985).
[7] F. P. Fehlner, *Low-Temperature Oxidation. The Role of Vitreous Oxides* (Wiley, New York, 1986).
[8] N. F. Mott, Philos. Mag. B **55**, 117 (1987).
[9] E. Irene, CRC Crit. Rev. Solid State Mater. Sci. **14**, 175 (1988).
[10] G. Lucovsky, J. F. Fitch, E. Kobeda, and E. Irene, in *The Physics and Chemistry of $SiO_2$ and the Si-$SiO_2$ Interface,* edited by C. R. Helms and D. E. Deal (Plenum, New York, 1988), p. 139.
[11] *The Si-$SiO_2$ System,* edited by P. Balk (Elsevier, Amsterdam, 1988).
[12] N. F. Mott, S. Rigo, F. Rochet, and A. M. Stoneham, Philos. Mag. B **60**, 189 (1989).
[13] F. J. Himpsel, D. A. Lapiano-Smith, J. F. Morar, and J. Bevk, in *The Physics and Chemistry of $SiO_2$ and the Si-$SiO_2$ Interface, II,* edited by C. R. Helms and B. E. Deal (Plenum, New York, 1993), p. 237.
[14] T. Engel, Surf. Sci. Rep. **18**, 91 (1993).
[15] C. R. Helms, and E. H. Poindexter, Rep. Prog. Phys. **57**, 791 (1994).
[16] F. J. Grunthaner and P. J. Grunthaner, Mater. Sci. Rep. **1**, 65 (1986).
[17] F. J. Himpsel, F. R. McFeely, A. Taleb-Ibrahimi, J. A. Yarmoff, and G. Hollinger, Phys. Rev. B **38**, 6084 (1988).
[18] V. D. Borman, E. P. Gusev, Yu. Yu. Lebedinski, and V. I. Troyan, Phys. Rev. B **49**, 5415 (1994).
[19] B. E. Deal and A. S. Grove, J. Appl. Phys. **36**, 3770 (1965).
[20] J. Blank, Philos. Mag. B **55**, 685 (1987).
[21] J. M. Delarious, C. R. Helms, D. B. Kao, and B. E. Deal, Appl. Surf. Sci. **39**, 89 (1989).
[22] H. Z. Massoud, J. D. Plummer, and E. A. Irene, J. Electrochem. Soc. **132**, 2693 (1985).
[23] A. M. Stoneham, C. R. M. Grovenor, and A. Cerezo, Philos. Mag. B **55**, 201 (1987).
[24] F. Rochet, S. Rigo, M. Froment, C. d'Anterroches, C. Maillot, H. Roulet, and G. Dufour, Adv. Phys. **35**, 339 (1986).
[25] F. J. Grunthaner, P. J. Grunthaner, R. P. Vasquez, B. F. Lewis, J. Maserjian, and A. Madhukar, Phys. Rev. Lett. **43**, 1683 (1979).
[26] G. Hollinger and F. J. Himpsel. Phys. Rev. B **28**, 3851 (1983).
[27] G. Hollinger, E. Bergignat, H. Chermette, F. Himpsel, D. Lopez, M. Lannoo, and M. Bensoussan, Philos. Mag. B **55**, 735 (1987).
[28] T. Hattori and K. Onishi, in *Interface Control of Electrical, Chemical, and Mechanical Properties,* edited by S. P. Murarka, K. Rose, T. Ohmi, and T. Seidel, MRS Symposia Proceedings No. 318 (Materials Research Society, Pittsburgh, 1994), p. 61.
[29] J. R. Engstrom, D. J. Bonser, and T. Engel, Surf. Sci. **268**, 238 (1992).
[30] V. D. Borman, E. P. Gusev, Yu. Yu. Lebedinski, and V. I. Troyan, Phys. Rev. Lett. **67**, 2387 (1991).
[31] J. M. Gibson and M. Y. Lanzerotti, Nature **340**, 128 (1989).
[32] F. M. Ross and J. M. Gibson, Phys. Rev. Lett. **68**, 1782 (1992).
[33] F. M. Ross, J. M. Gibson, and R. D. Twesten, Surf. Sci. **310**, 243 (1994).
[34] R. D. Twesten, J. M. Gibson, and F. M. Ross, MRS Bull. **29**, 38 (1994).
[35] T. Horie, Y. Takakuwa, and N. Miyamoto, Jpn. J. Appl. Phys. **33**, 4684 (1994).
[36] A. Feltz, U. Memmert, and R. J. Behm, Surf. Sci. **314**, 34 (1994).
[37] L. C. Feldman, P. J. Silverman, J. S. Williams, T. E. Jackman, and I. Stensgaard, Phys. Rev. Lett. **41**, 1396 (1978).
[38] R. Haight and L. C. Feldman, J. Appl. Phys. **53**, 4884 (1982).
[39] Q. Liu, J. F. Wall, and E. A. Irene, J. Vac. Sci. Technol. A **12**, 2625 (1994).
[40] R. H. Doremus and S. C. Kao, in *Interface Control of Electrical, Chemical, and Mechanical Properties* (Ref. 28), p. 53.
[41] P. Morgen, U. Hoffer, W. Wurth, and E. Umbach, Phys. Rev. B **39**, 3720 (1989).
[42] M. M. Banaszak-Holl, S. Lee, and F. R. McFeely, Appl. Phys. Lett. **65**, 1097 (1994).
[43] H. Kageshima and M. Tabe, in *Control of Semiconductor Interfaces,* edited by I. Ohdomari, M. Oshima, and A. Hiraki (Elsevier, Amsterdam, 1994), p. 227.
[44] A. Ourmazd, D. W. Taylor, J. A. Rentscheir, and J. Bevk, Phys. Rev. Lett. **53**, 743 (1987).
[45] P. H. Fouss, H. J. Norton, S. Brennan, and A. Fisher-Colbrie, Phys. Rev. Lett. **60**, 600 (1988).
[46] T. Yamazaki, S. Miyazaki, C. H. Bjorkman, M. Fukuda, and M. Hirose, in *Interface Control of Electrical, Chemical, and Mechanical Properties* (Ref. 28).
[47] W. A. Tiller, J. Electrochem. Soc. **128**, 689 (1981).
[48] S. T. Dunham and J. D. Plummer, J. Appl. Phys. **59**, 2541 (1986).
[49] K. Taniguchi, Y. Shibata, and C. Hamaguchi, J. Appl. Phys.

**65**, 2723 (1989).
[50]J. J. Lander and J. Morrison, J. Appl. Phys. **33**, 2089 (1962).
[51]F. W. Smith and G. Ghidini, J. Electrochem. Soc. **129**, 1300 (1982).
[52]R. E. Walkup and S. Raider, Appl. Phys. Lett. **53**, 888 (1988).
[53]J. Seiple and J. P. Pelz, Phys. Rev. Lett. **73**, 999 (1994).
[54]R. Tromp, G. W. Rubloff, P. Balk, F. K. DeGoues, and E. J. van Loenen, Phys. Rev. Lett. **55**, 2332 (1985).
[55]L. C. Feldman, J. W. Mayer, and S. T. Picraux, *Materials Analysis by Ion Channeling* (Academic, New York, 1982).
[56]J. F. van der Veen, Surf. Sci. Rep. **5**, 199 (1985).
[57]P. Fenter and T. Gustafsson, Phys. Rev. B **43**, 12 195 (1991).
[58]P. Statiris, H. C. Lu, and T. Gustafsson, Phys. Rev. Lett. **72**, 3574 (1994).
[59]E. P. Gusev, H. C. Lu, T. Gustafsson, and E. Garfunkel, in *Interface Control of Electrical, Chemical, and Mechanical Properties* (Ref. 28), p. 69.
[60]R. M. Tromp and E. J. van Loenen, Surf. Sci. **155**, 441 (1985).
[61]L. C. Feldman, in *The Physics and Chemistry of $SiO_2$ and the Si-$SiO_2$ Interface* (Ref. 10), p. 199.
[62]L. C. Feldman, Surf. Sci. **299/300**, 233 (1994).
[63]N. W. Cheung, L. C. Feldman, P. J. Silverman, and I. Stensgaard, Appl. Phys. Lett. **35**, 859 (1979).
[64]F. C. Stedile, I. J. R. Baumvol, J. J. Ganem, S. Rigo, I. Trimaille, G. Battistig, W. H. Schulte, and H. W. Becker, Nucl. Instrum. Methods Phys. Res. Sect. B **85**, 248 (1994).
[65]S. S. Crity and J. B. Condon, J. Electrochem. Soc. **128**, 2170 (1981).
[66]F. Rochet, B. Agius, and S. Rigo, J. Electrochem. Soc. **131**, 914 (1984).
[67]J. A. Costello and R. E. Tressler, J. Electrochem. Soc. **131**, 1944 (1984).
[68]C. J. Han and C. R. Helms, J. Electrochem. Soc. **135**, 1824 (1988).
[69]I. Trimaille and S. Rigo, Appl. Surf. Sci. **39**, 65 (1989).
[70]M. P. Murrell, C. J. Sofield, and S. Sugden, Philos. Mag. B **63**, 1277 (1991).
[71]J. J. Ganem, G. Battistig, S. Rigo, and I. Trimaille, Appl. Surf. Sci. **65/66**, 647 (1993).
[72]R. M. Tromp, M. Copel, M. C. Reuter, M. Horn von Hoegen, J. Speidell, and R. Koudijs, Rev. Sci. Instrum. **62**, 2679 (1991).
[73]H. H. Andersen and J. F. Ziegler, *The Stopping and Ranges of Ions in Matter* (Pergamon, New York, 1977), Vol. 3.
[74]G. K. Kinchin and R. S. Pease, Rep. Prog. Phys. **18**, 1 (1955).
[75]H. Niehus, W. Heiland, and E. Taglauer, Surf. Sci. Rep. **17**, 213 (1992).
[76]E. Taglauer, Surf. Sci. **299/300**, 64 (1994).
[77]H. Dallaporta, M. Liehr, and J. E. Lewis, Phys. Rev. B **41**, 5075 (1990).
[78]H. C. Lu, T. Gustafsson, E. P. Gusev, and E. Garfunkel (unpublished).
[79]M. Tabe, T. T. Chiang, I. Lindau, and W. E. Spicer, Phys. Rev. B **34**, 2706 (1986).
[80]F. G. Himpsel, Surf. Sci. **299/300**, 525 (1994).
[81]M. F. Hochella and A. H. Carim, Surf. Sci. **197**, L260 (1988).
[82]J. E. Fulghum, R. Stokell, G. McGuire, B. Patnaik, N. Yu, Y. J. Zhao, and N. Parikh, J. Electron. Spectrosc. Relat. Phenom. **60**, 117 (1992).
[83]W. N. Lennard, G. R. Massoumi, I. V. Mitchell, H. T. Tang, and D. F. Mitchell, Nucl. Instrum. Methods Phys. Res. Sect. B **85**, 42 (1994).
[84]C. J. McHargue, D. L. Joslin, and C. M. White, Nucl. Instrum. Methods Phys. Res. Sect. B **91**, 549 (1994).
[85]P. E. Batson, N. D. Browning, and D. A. Muller, Microsc. Soc. Am. Bull. **24**, 371 (1994).
[86]P. E. Batson, Nature **366**, 727 (1993).
[87]S. M. Goodnick, D. K. Ferry, C. M. Wilmsen, Z. Liliental, D. Fathy, and O. L. Krivanek, Phys. Rev. B **32**, 8171 (1985).
[88]H. Akutsu, Y. Sami, and I. Ohdomari, Phys. Rev. B **44**, 1616 (1991).
[89]V. A. Yakovlev, Q. Liu, and E. Irene, J. Vac. Sci. Technol. B **10**, 427 (1992).
[90]E. Irene, Thin Solid Films **233**, 96 (1993).
[91]E. P. Gusev, H. C. Lu, E. Garfunkel, T. Gustafsson, and V. A. Yakovlev (unpublished).
[92]T. Dutta and N. M. Ravindra, Phys. Status Solidi **134**, 447 (1992).
[93]S. C. Kao and R. H. Doremus, in *The Physics and Chemistry of $SiO_2$ and the Si-$SiO_2$ Interface II* (Ref. 13), p. 23.
[94]M. Morita, T. Ohmi, E. Hasegawa, M. Kawakami, and K. Suma, Appl. Phys. Lett. **55**, 562 (1989).
[95]A. Stockhausen, T. U. Kampen, and W. Monch, Appl. Surf. Sci. **56-58**, 795 (1992).
[96]J. Westermann, H. Nienhaus, and W. Monch, Surf. Sci. **311**, 101 (1994).
[97]U. Neuwald, U. Memmert, and R. J. Behm, in *Proceedings of the 41st American Vacuum Society Symposium* (American Vacuum Society, Denver, CO, 1994), p. 177.
[98]M. Morita, T. Ohmi, E. Hasegawa, M. Kawakami, and M. Ohwada, J. Appl. Phys. **68**, 1272 (1990).
[99]M. Morita and T. Ohmi, Jpn. J. Appl. Phys. **33**, 370 (1994).
[100]M. Hirose, T. Yasaka, and S. Miyazaki, Semicond. Res. **36**, 263 (1991).
[101]K. Onishi and T. Hattori, Jpn. J. Appl. Phys. **33**, L676 (1994).
[102]N. M. Ravindra, J. Narayan, D. Fathy, J. K. Stivastava, and E. A. Irene, J. Mater. Res. **2**, 216 (1987).
[103]E. P. Gusev and E. Garfunkel (unpublished).
[104]M. Suzuki, Y. Homma, Y. Kudoh, and N. Yabumoto, Jpn. J. Appl. Phys. **32**, 1419 (1993).
[105]M. Niwa, M. Udagawa, K. Okada, T. Kouzazki, and R. Sinclair, Appl. Phys. Lett. **63**, 675 (1993).
[106]A. Diebold and B. Doris, Surf. Interface Appl. **20**, 127 (1993).
[107]J. E. Griffith and D. A. Grigg, J. Appl. Phys. **74**, R83 (1993).
[108]S. D. Kosowsky, C. H. Hsu, P. S. Pershan, J. Bevk, and B. S. Freer, Appl. Surf. Sci. **84**, 179 (1995).
[109]M. M. Banaszak-Holl and F. R. McFeely, Phys. Rev. Lett. **71**, 2441 (1993).
[110]Z. H. Lu, M. J. Graham, D. T. Jiang, and K. H. Tan, Appl. Phys. Lett. **63**, 2941 (1993).
[111]A. Pasquarello, M. S. Hybertsen, and R. Car, Phys. Rev. Lett. **74**, 1024 (1995).
[112]J. Seiple, J. Pecquet, Z. Meng, and J. P. Pelz, J. Vac. Sci. Technol. A **11**, 1649 (1993).
[113]M. P. D'Evelyn, M. M. Nelson, and T. Engle, Surf. Sci. **186**, 75 (1987).
[114]B. Leroy, Philos. Mag. B **55**, 159 (1987).
[115]T. Tamura, N. Tanaka, M. Tagawa, N. Ohmae, and M. Umeno, Jpn. J. Appl. Phys. **32**, 12 (1993).
[116]S. M. Hu, J. Appl. Phys. **45**, 1567 (1974).
[117]D. G. Cahill and Ph. Avouris, Appl. Phys. Lett. **60**, 326 (1992).
[118]M. Udagawa, M. Niwa, and I. Sumita, Jpn. J. Appl. Phys. **32**, 282 (1993).
[119]K. Wurm, R. Kliese, Y. Hong, B. Rottger, Y. Wei, H. Neddermeyer, and I. S. T. Tsong, Phys. Rev. B **50**, 1567

(1994).
[120]G. Renaud, P. H. Fouss, A. Ourmazd, J. Bevk, and B. S. Freer, Appl. Phys. Lett. **58**, 1044 (1991).
[121]T. A. Rabedeau, I. M. Tidswell, P. S. Pershan, J. Berk, and B. S. Freer, Appl. Phys. Lett. **59**, 3422 (1991).
[122]G. Lupke, D. J. Bottomley, and H. M. van Driel, Phys. Rev. B **47**, 10 389 (1993).
[123]Y. Ono, M. Tabe, and H. Kageshima, Phys. Rev. B **48**, 14 291 (1993).
[124]P. Jakob, Y. J. Chabal, K. Raghavachari, and S. B. Christman, Phys. Rev. B **47**, 6839 (1993).
[125]G. S. Higashi and Y. J. Chabal, in *Handbook of Silicon Wafer Cleaning Technology,* edited by W. Kern (Noyes, Park Ridge, NJ, 1993), p. 433.
[126]T. Ohmi, Proc. IEEE **81**, 716 (1993).
[127]G. Molière, Z. Naturforsch. Teil A **2**, 133 (1947).
[128]*High Energy Ion Beam Analysis and Solids,* edited by G. Gotz and K. Gartner (Akademie-Verlag, Berlin, 1988).
[129]P. Sigmund, Nucl. Instrum. Methods Phys. Res. Sect. B **85**, 541 (1994).
[130]F. Besenbacher, J. Andersen, and E. Bonderup, Nucl. Instrum. Methods **168**, 1 (1980).
[131]P. F. A. Alkemade, W. C. Turkenburg, and W. F. van der Weg, Nucl. Instrum. Methods. Phys. Res. Sect. B **28**, 161 (1987).
[132]Y. Kido and T. Koshikawa, Phys. Rev. A **44**, 1759 (1991).
[133]N. Bohr, K. Dan. Vidensk. Selsk. Mat. Fys. Medd. **18**, 8 (1948).
[134]J. Lindhard and M. Scharff, K. Dan. Vidensk. Mat. Fys. Medd. **27**, 15 (1953).
[135]J. Lindhard and M. Scharff, Phys. Rev. **124**, 128 (1961).